International Journal of Minerals, Metallurgy and Materials
Volume 30, Number 7, July 2023, Page 1363
https://doi.org/10.1007/s12613-023-2618-5

Fabrication of g-C_3N_4 nanosheet/Bi_5O_7Br/NH_2-MIL-88B (Fe) nanocomposites: Double S-scheme photocatalysts with impressive performance for the removal of antibiotics under visible light

Nasrin Sedaghati[1)], *Aziz Habibi-Yangjeh*[1),✉], *and Alireza Khataee*[2,3)]

1) Department of Chemistry, Faculty of Science, University of Mohaghegh Ardabili, Ardabil 56199-11367, Iran
2) Research Laboratory of Advanced Water and Wastewater Treatment Processes, Department of Applied Chemistry, Faculty of Chemistry, University of Tabriz, Tabriz 51666-16471, Iran
3) Department of Environmental Engineering, Faculty of Engineering, Gebze Technical University, Gebze 41400, Turkey
(Received: 3 November 2022; revised: 30 January 2023; accepted: 21 February 2023)

Abstract: Novel graphitic carbon nitride (g-C_3N_4) nanosheet/Bi_5O_7Br/NH_2-MIL-88B (Fe) photocatalysts (denoted as GCN-NSh/Bi_5O_7Br/Fe-MOF, in which MOF is metal–organic framework) with double S-scheme heterojunctions were synthesized by a facile solvothermal route. The resultant materials were examined by X-ray photoelectron spectrometer (XPS), X-ray diffraction (XRD), scanning electron microscopy (SEM), energy dispersive X-ray spectroscopy (EDX), transmission electron microscopy (TEM), high-resolution transmission electron microscopy (HRTEM), photoluminescence spectroscopy (PL), Fourier transform infrared spectroscopy (FT-IR), UV-Vis diffuse reflection spectroscopy (UV-vis DRS), photocurrent density, electrochemical impedance spectroscopy (EIS), and Brunauer–Emmett–Teller (BET) analyses. After the integration of Fe-MOF with GCN-NSh/Bi_5O_7Br, the removal constant of tetracycline over the optimal GCN-NSh/Bi_5O_7Br/Fe-MOF (15wt%) nanocomposite was promoted 33 times compared with that of the pristine GCN. The GCN-NSh/Bi_5O_7Br/Fe-MOF (15wt%) nanocomposite showed superior photoactivity to azithromycin, metronidazole, and cephalexin removal that was 36.4, 20.2, and 14.6 times higher than that of pure GCN, respectively. Radical quenching tests showed that $^{\bullet}O_2^-$ and h^+ mainly contributed to the elimination reaction. In addition, the nanocomposite maintained excellent activity after 4 successive cycles. Based on the developed n–n heterojunctions among n-GCN-NSh, n-Bi_5O_7Br, and n-Fe-MOF semiconductors, the double S-scheme charge transfer mechanism was proposed for the destruction of the selected antibiotics.

Keywords: g-C_3N_4 nanosheet/Bi_5O_7Br/NH_2-MIL-88B (Fe); metal–organic framework; double S-scheme heterojunctions; antibiotics; photocatalytic performance

1. Introduction

Global population growth and numerous industrialization have a major impact on water pollution, which is one of the most important environmental crises. The main source of this pollution is the uncontrolled release of various organic pollutants, including antibiotics, pesticides, herbicides, antiparasites, and organic dyes, into aquatic systems [1]. Therefore, developing efficacious technology is imperative to thoroughly eliminate these pollutants from our environment [2]. Numerous physicochemical and biological methods developed for water decontamination have some bottlenecks of difficulty in scaling up, complicated operational systems, and high cost [3]. Among these treatment technologies, advanced oxidation processes using heterogeneous photocatalysts have attracted interest owing to their ability to work at ambient conditions, cheap operational cost, and utilization of solar energy as a sustainable energy source [4–5].

Graphitic carbon nitride (g-C_3N_4) has recently been considered as one of the most promising heterogeneous photocatalysts due to its appealing advantages, including remarkable stability, biocompatibility, nontoxicity, low price, facile large-scale preparation, and middle band energy [6–8]. Nevertheless, g-C_3N_4 suffers from a large number of disadvantages, including poor surface area, small segregation of photoexcited e^-/h^+ pairs, and limited visible-light absorption [6]. Hence, many researches have been conducted on the synthesis of mesoporous structures, doping of different elements, and constructing heterojunctions with various semiconductors. Furthermore, nonstoichiometric bismuth-rich oxyhalides have attracted considerable interest for utilization as heterogeneous photocatalysts due to their attractive features of high stability, suitable energy gap, and tunable light absorption range [9]. As a nonstoichiometric bismuth-based oxyhalide semiconductor, Bi_5O_7Br has shown fascinating features of unique layered crystal structure, high chemical stability, and wide visible-light response [10].

Metal–organic frameworks (MOFs) have a porous struc-

✉ Corresponding author: Aziz Habibi-Yangjeh E-mail: ahabibi@uma.ac.ir

ture and consist of cationic nodes and organic linkers [11]. These promising materials have presented a wide range of applications such as energy storage, drug delivery, cancer therapy, photocatalysis, and greenhouse gas capture [12]. Despite their tunable porous structures, wide visible-light-harvesting ability, and high specific surface, they suffer from the fast recombination of photoinduced charges and poor stability and conductivity [13–14]. Constructing a heterojunction with other semiconductors is one of the superior methods to improve their photocatalytic performances and overcome the above disadvantages [15].

We report novel ternary photocatalysts exhibiting impressive activity synthesized through the integration of g-C_3N_4 nanosheets with Bi_5O_7Br and NH_2-MIL-88B (Fe) as a Fe-MOF. The fabricated double S-scheme heterojunction photocatalysts displayed exceptional performance in the photocatalytic removal of tetracycline hydrochloride (TC), metronidazole (MET), cephalexin (CFX), and azithromycin (AZY) antibiotics under visible-light illumination. The integrated n-type g-C_3N_4, Bi_5O_7Br, and NH_2-MIL-88B (Fe) semiconductors formed n-n heterojunctions, which played a significant role in the segregation of the charges and produced more reactive species, resulting in exceptional photocatalytic activity.

2. Experimental

2.1. Fabrication of materials

g-C_3N_4 (GCN) and g-C_3N_4 nanosheet (GCN-NSh) were synthesized as previously described [16]. For the synthesis of GCN-NSh/Bi_5O_7Br (30wt%) photocatalyst, where 30wt% is the weight percentage of Bi_5O_7Br, 0.35 g of GCN-NSh was sonicated for 10 min in 100 mL of water. Meanwhile, 0.294 g of bismuth nitrate ($Bi(NO_3)_3{\cdot}5H_2O$) was dissolved in 50 mL of water and added to the suspension. After stirring for 60 min, 0.012 g of NaBr (dissolved in 40 mL of water) was slowly appended to the above system. The pH was set to 8 by the addition of NaOH. After stirring for 3 h, the resultant product was rinsed with ethanol and water and dried at about 60°C overnight. Other GCN-NSh/Bi_5O_7Br nanocomposites with different compositions of Bi_5O_7Br (10wt%, 20wt%, and 40wt%) were prepared under the same conditions for comparison.

The synthesis of GCN-NSh/Bi_5O_7Br/NH_2-MIL-88B (Fe) nanocomposites (denoted as GCN-NSh/Bi_5O_7Br/Fe-MOF) was performed using a solvothermal method. For the preparation of GCN-NSh/Bi_5O_7Br/Fe-MOF (15wt%) nanocomposite, 0.425 g of GCN-NSh/Bi_5O_7Br (30wt%), 0.056 g of 2-aminoterephthalic acid (H_2ATA), and 0.084 g of $FeCl_3{\cdot}6H_2O$ in 70 mL of N,N-dimethylformamide (DMF) were sonicated for 30 min. Thereafter, the suspension was autoclaved at 130°C for 24 h. In the last step, the slurry was rinsed out with ethanol and water and dried at 60°C. The GCN-NSh/Bi_5O_7Br/Fe-MOF nanocomposites with different compositions of Fe-MOF (5wt%, 10wt%, and 20wt%) were synthesized with the same procedure. The method utilized for the fabrication of GCN-NSh/Bi_5O_7Br/Fe-MOF nanocomposites is depicted in Scheme 1.

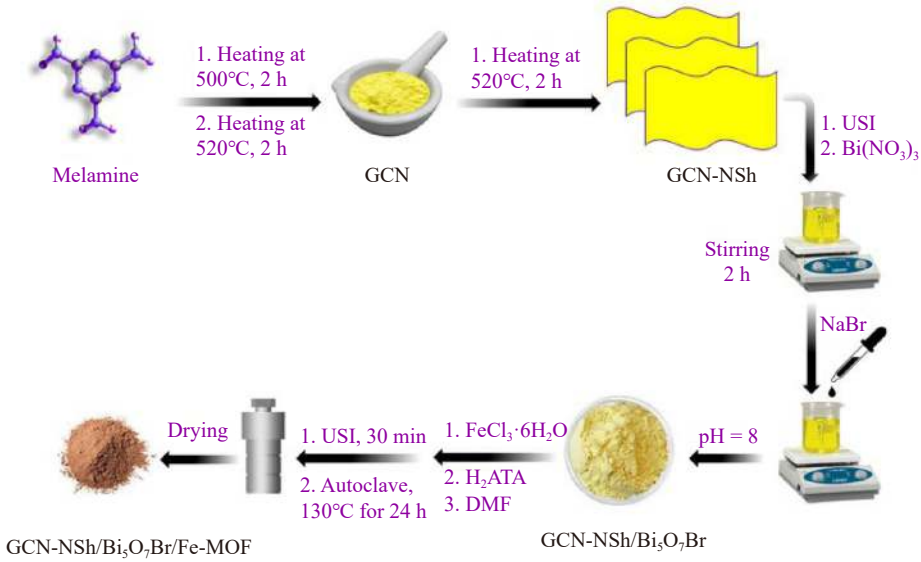

Scheme 1. Preparation procedure for GCN-NSh/Bi_5O_7Br/Fe-MOF nanocomposites.

2.2. Characterization

XRD data were obtained using an X-ray diffractometer with Cu K_α radiation (Philips X'pert). HRTEM and TEM images used for microstructure analysis were acquired with a Talos F200S microscope (Thermo Scientific). N_2 sorption data were assessed using a BELSORP mini II instrument. FT-IR spectra were recorded with a Perkin Elmer spectrometer. EDX spectra and SEM images were obtained by a Mira 3 MIRA3 FEG-SEM analyzer. PL analyses were performed with an Agilent fluorescence spectrophotometer. UV-visible DR spectra were measured with a Scinco 4100 spectrophotometer. XPS spectra were obtained via a PHI 5000 Versa Probe II XPS instrument. Electrochemical data were

recorded on an Autolab PGSTAT302N EIS analyzer. Ultrasound irradiation was executed with an HD 3100 ultrasound processor. Optical absorptions were recorded by a Nanomabna spectrophotometer.

2.3. Evaluation of photoactivity

Photocatalytic performances were studied at 25°C under visible light supplied by 50 W LED. In brief, 200 mL of TC (6.75×10^{-5} M), MET (7.01×10^{-5} M), CFX (5.75×10^{-5} M), and AZY (2.54×10^{-5} M) were monitored at wavelength of 357, 320, 261, and 208 nm. Details about photocatalysis tests were described in the previous study [17].

3. Results and discussion

Phase structures were examined by XRD patterns, and the outcomes are presented in Fig. 1(a). The distinct peaks of GCN and GCN-NSh materials are identified at 13° and 27.4°, which are related to the (100) and (002) planes, respectively, implying in-planar and interlayer stacking reflections (JCPDS PDF No. 87-1526) [18]. The lower intensity of the peaks in GCN-NSh compared with the bulk one indicates that GCN-NSh has reduced thickness and has been considerably exfoliated [19]. For the diffraction peaks of GCN-NSh/Bi_5O_7Br (30wt%) nanocomposite, the peaks of Bi_5O_7Br or-

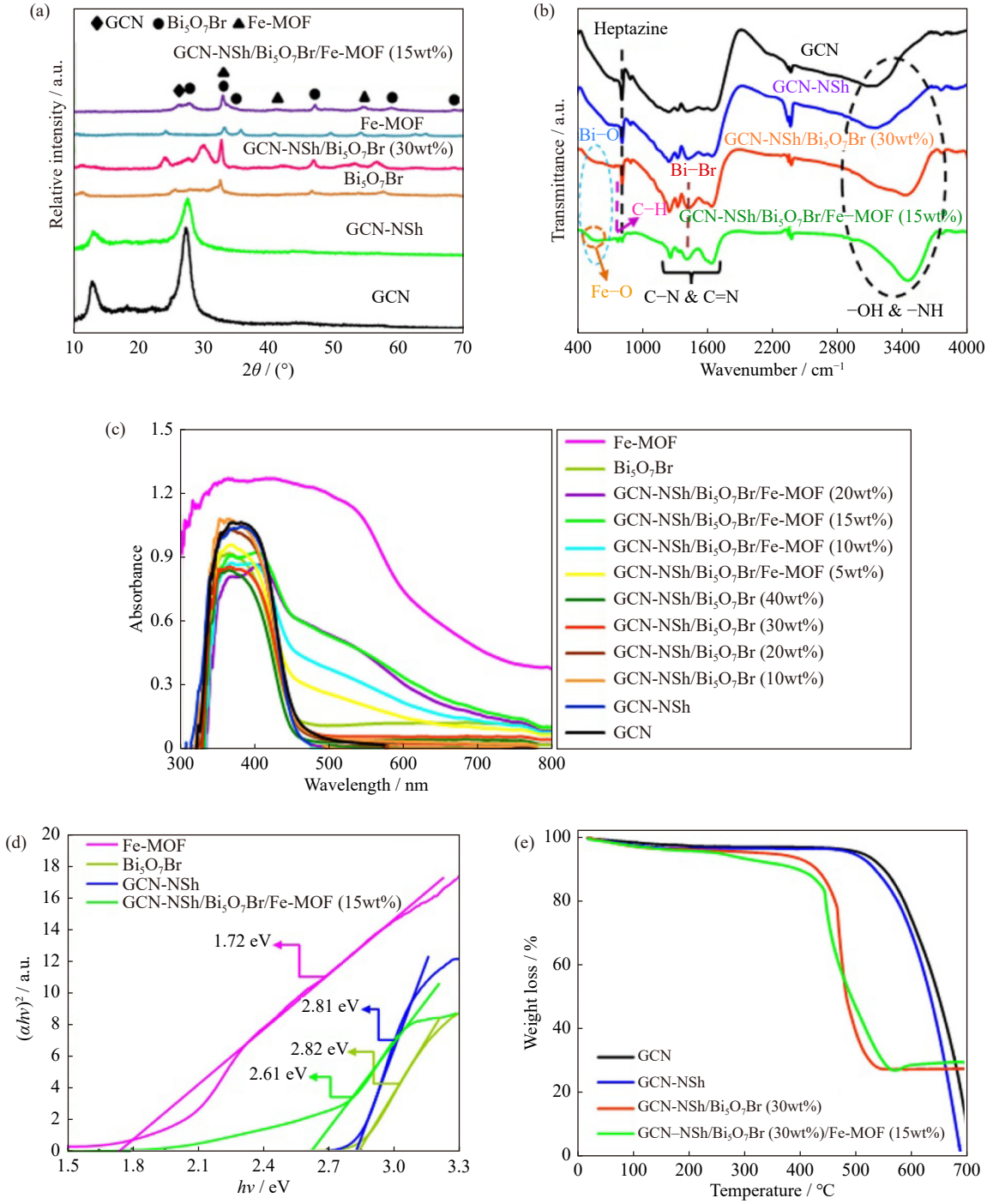

Fig. 1. (a) XRD, (b) FT-IR, (c) UV-vis DRS, (d) Tauc plots, and (e) TG analysis for the selected photocatalysts.

thorhombic phase were detected (JCPDS PDF No. 38-0493) in addition to the peaks of GCN-NSh [20]. For the ternary GCN-NSh/Bi_5O_7Br/Fe-MOF (15wt%) nanocomposite, a series of characteristic peaks of Fe-MOF was observed (Cambridge crystallographic data center: 647646) [21] along with the diffraction peaks of GCN-NSh and Bi_5O_7Br components, denoting the successful production of GCN-NSh/Bi_5O_7Br/Fe-MOF (15wt%) nanocomposite. After the integration of Fe-MOF with GCN-NSh/Bi_5O_7Br (30wt%) nanocomposite, the peak related to the GCN-NSh component shifted due to the changing interlayer spacing of the GCN-NSh layered structure [22]. Accordingly, the XRD results affirmed the successful preparation of GCN-NSh/Bi_5O_7Br/Fe-MOF (15wt%) nanocomposite without impurity peaks.

The FT-IR spectra of photocatalysts were depicted to identify the structures and their functional groups (Fig. 1(b)). The band at 810 cm^{-1} is ascribed to the heptazine units, and the peaks observed at 1100–1700 cm^{-1} are allocated to the C=N and C–N groups from the GCN and GCN-NSh components [23–24]. Moreover, the broad peaks at 3000–3300 cm^{-1} are ascribed to the O–H and N–H stretching vibrations derived from the adsorbed H_2O [25]. The absorption bands at 504 and 1400 cm^{-1} in the spectra of Bi_5O_7Br-based photocatalysts are ascribed to the vibrations of Bi–O and Bi–Br bonds, respectively [26]. The peaks at 1255 and 769 cm^{-1} correspond to the C–N group stretching and C–H bending vibration of the benzene ring, respectively [27]. In addition, the peak at 541 cm^{-1} is relevant to Fe–O bond stretching [28].

Light absorption abilities were evaluated, and the results are presented in Fig. 1(c). A blue shift occurred in the spectrum of GCN-NSh compared with that of the bulk one, which is relevant to the quantum confinement effect resulting from the exfoliation of GCN [16]. After the combination of Fe-MOF with GCN-NSh/Bi_5O_7Br (30wt%), the intensity of absorption in the visible region significantly increased. This phenomenon is attributed to the supreme visible-light absorption capability of Fe-MOF nanocomposites. The relevant optical gaps of the materials were calculated by Tauc plots as presented in Fig. 1(d). The band gaps of GCN-NSh/Bi_5O_7Br/Fe-MOF (15wt%), GCN-NSh, Bi_5O_7Br, and Fe-MOF samples were estimated to be 2.61, 2.81, 2.82, and 1.72 eV, respectively [16,29–30]. TG analyses were performed to review the thermal stability of GCN, GCN-NSh, GCN-NSh/Bi_5O_7Br (30wt%), and GCN-NSh/Bi_5O_7Br/Fe-MOF (15wt%) photocatalysts from 20 to 700°C, and the outcomes are shown in Fig. 1(e). A slight weight loss was observed up to 140°C because of the evaporation of water molecules adsorbed on the materials. Thereafter, a significant weight loss started after almost 400°C, which is assigned to the combustion of the graphitic carbon nitride component of the samples [31–32]. When Bi_5O_7Br and Fe-MOF particles were anchored on GCN-NSh, the combustion stage started at lower temperatures compared with those for GCN and GCN-NSh photocatalysts. Ultimately, the weight percentages of GCN-NSh in the GCN-NSh/Bi_5O_7Br (30wt%) and GCN-NSh/Bi_5O_7Br/Fe-MOF (15wt%) nanocomposites were calculated to be about 70% and 68%, respectively.

The shape and morphology of GCN, GCN-NSh, Bi_5O_7Br, Fe-MOF, and GCN-NSh/Bi_5O_7Br/Fe-MOF (15wt%) samples were observed through SEM analyses as shown in Fig. 2(a–e), respectively. As displayed in the SEM and TEM images of GCN-NSh/Bi_5O_7Br/Fe-MOF (15wt%) samples (Fig. 2(e–f)), Bi_5O_7Br and Fe-MOF nanoparticles were well stacked over GCN-NSh. The HRTEM image (Fig. 2(g)) showed the lattice fringe spacings of 0.326, 0.320, and 0.35 nm were well matched to the (002) plane of GCN-NSh, (312) plane of Bi_5O_7Br, and (001) plane of Fe-MOF, respectively, proving the existence of heterojunctions among GCN-NSh, Bi_5O_7Br, and Fe-MOF [33–35]. EDX spectroscopy was utilized to analyze the elemental composition of GCN-NSh/Bi_5O_7Br/Fe-MOF (15wt%) nanocomposite. Fig. 2(h) showed C, N, O, Fe, Br, and Bi elements in the photocatalyst. Other peaks related to the elements applied for the sputter coating of the photocatalyst appeared on the EDX stage. Furthermore, Fig. 2(i) ascertained the homogeneous distribution of elements in the GCN-NSh/Bi_5O_7Br/Fe-MOF (15wt%) nanocomposite, confirming the purity of the ternary photocatalyst.

XPS studies were conducted to study the chemical state of the elements in the GCN-NSh/Bi_5O_7Br/Fe-MOF (15wt%) sample. Fig. 3(a) displayed C, N, O, Fe, Br, and Bi elements in the photocatalyst, which well agrees with the EDX analyses in Fig. 2(i). The high-resolution C1s spectrum showed three peaks at 284.6, 286.1, and 288.5 eV, as shown in Fig. 3(b). The peak at 284.6 eV was relevant to the carbon in the benzene ring, such as sp^2 C–C and C–H groups [36]. Furthermore, the peak at 288.5 eV corresponded to the bonded carbon in the O–C=O group from the H_2ATA linker or the sp^2 hybridized carbon bonded to the N of the triazine rings [37–38]. In addition, the peak at 286.1 eV was relevant to the C–N–C group of g-C_3N_4 [39]. Fig. 3(c) showed the three splitting peaks of 398.7, 399.9, and 401.2 eV, which were matched to the sp^2 hybridized N atoms in the C=N–C and sp^3 hybridized nitrogen in the N–$(C)_3$ and –NH_2, respectively [40–41]. Fig. 3(d) presented two peaks at 158.91 and 164.21 eV, which are devoted to Bi $4f_{5/2}$ and Bi $4f_{7/2}$, respectively [42]. The O 1s spectrum indicates the peaks at 529.6 and 531.4 eV, which belong to the oxygen of Bi_5O_7Br and water molecules, respectively (Fig. 3(e)) [20]. The spectrum of Br $3p_{3/2}$ and Br $3p_{1/2}$ at about 181.9 and 188.6 eV indicated the presence of Br^- in the Bi_5O_7Br component [43] (Fig. 3(f)). The Fe 2p spectrum (Fig. 3(g)) can be splitted into two peaks at 710 and 722.8 eV, which were relevant to the Fe $2p_{3/2}$ and Fe $2p_{1/2}$ from Fe^{3+}, respectively. Moreover, the satellite peak at 718 eV affirmed the presence of Fe^{3+} in the GCN-NSh/Bi_5O_7Br/Fe-MOF (15wt%) nanocomposite [44].

PL and EIS spectra were conducted to peruse the efficiency of electron/hole pairs separation, migration, and transfer. Usually, the low PL intensity shows a large segregation efficacious of the charges. As in Fig. 4(a), the weakest PL intensity was relevant to the GCN-NSh/Bi_5O_7Br/Fe-MOF

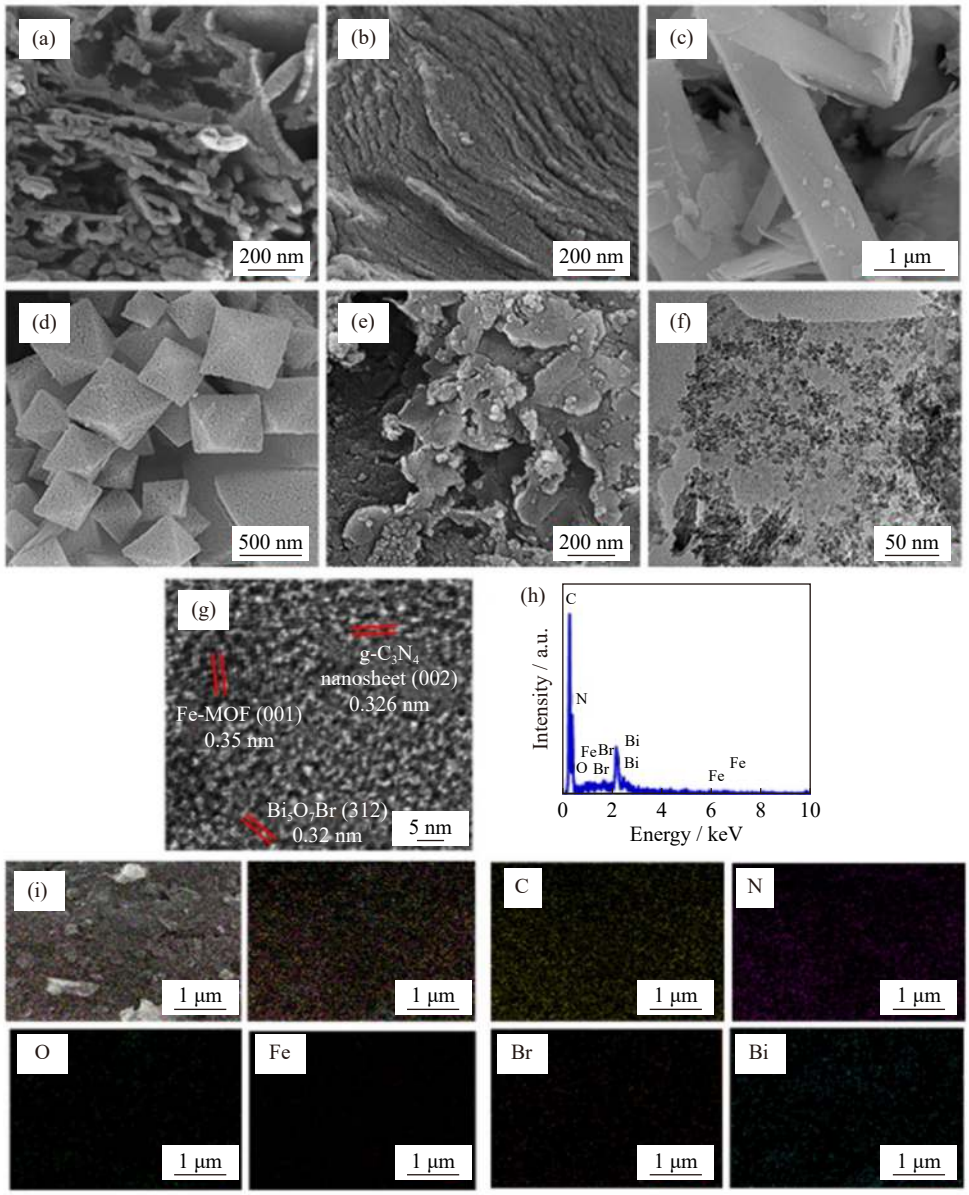

Fig. 2. SEM images of (a) GCN, (b) GCN-NSh, (c) Bi_5O_7Br, (d) Fe-MOF, and (e) GCN-NSh/Bi_5O_7Br/Fe-MOF (15wt%) photocatalysts. (f) TEM, (g) HRTEM, (h) EDX spectrum, and (i) EDX elemental mapping analysis for GCN-NSh/Bi_5O_7Br/Fe-MOF (15wt%) photocatalyst.

(15wt%) nanocomposite, which affirmed the high segregation capability of electron/hole pairs. EIS measurements were implemented for the synthesized materials to investigate the charge migration and transfer efficacious. The Nyquist plots for GCN, GCN-NSh, Bi_5O_7Br, GCN-NSh/Bi_5O_7Br (30wt%), and GCN-NSh/Bi_5O_7Br/Fe-MOF (15wt%) photocatalysts were shown in Fig. 4(b). The GCN-NSh/Bi_5O_7Br/Fe-MOF (15wt%) nanocomposite showed the smallest arc radius compared with the pure and binary samples, affirming the least electron/hole pair movement resistance in the ternary nanocomposite. In addition to the above results, photocurrent intensities were evaluated for some on–off cycles, and the outcomes are illustrated in Fig. 4(c). As expected, the GCN-NSh/Bi_5O_7Br/Fe-MOF (15wt%) photocatalyst exhibited the highest photocurrent responses among the materials, indicating that it has the least recombination for the charge carriers. Therefore, the UV-vis DRS, PL, EIS, and photocurrent outcomes confirmed that the promoted performance of the ternary GCN-NSh/Bi_5O_7Br/Fe-MOF (15wt%) nanocomposite is attributed to the formation of abundant charge carriers under visible light, effective segregation of charges, and less resistance for charge transfer among the components, leading to improved photocatalytic performance. The BET of the samples was evaluated by nitrogen sorption, and the results showed that the isotherms are type II with H3 hysteresis hoops, affirming mesoporous structure (Fig. 4(d)). The surface areas were reported to be 31.4 and 54.9 $m^2 \cdot g^{-1}$ for the GCN-NSh/Bi_5O_7Br (30wt%) and GCN-NSh/Bi_5O_7Br/Fe-MOF (15wt%), respectively (Table 1). Compared with the surface area of GCN-NSh (88.1 $m^2 \cdot g^{-1}$), the surface area of GCN-NSh/Bi_5O_7Br (30wt%) decreased due to surface blocking after integration with Bi_5O_7Br [16]. After the integration of Fe-MOF with GCN-NSh/Bi_5O_7Br (30wt%), the surface area was significantly improved.

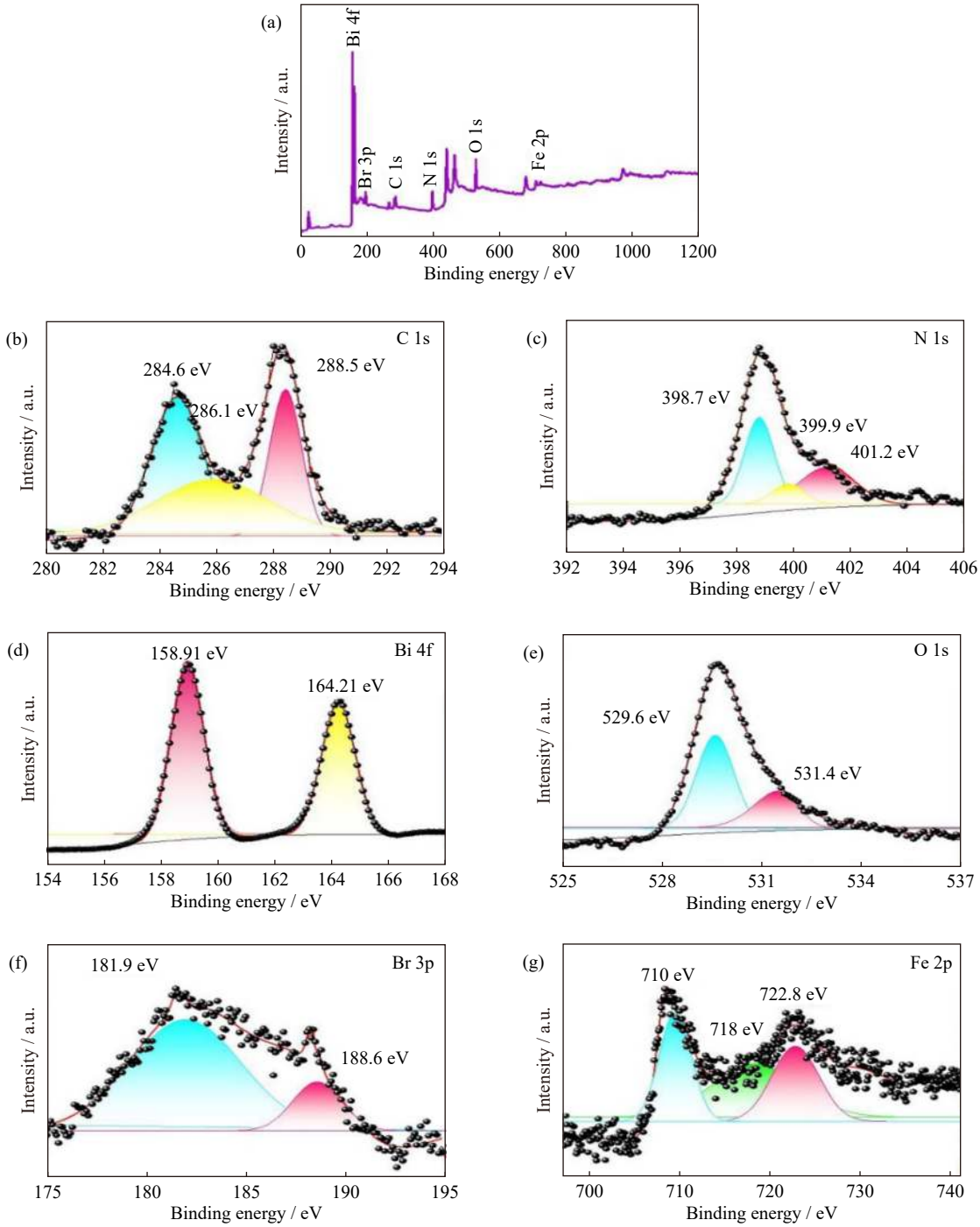

Fig. 3. XPS spectra for GCN-NSh/Bi_5O_7Br/Fe-MOF (15wt%) nanocomposite: (a) survey; (b) C 1s; (c) N 1s; (d) Bi 4f; (e) O 1s; (f) Br 3p; (g) Fe 2p.

Fig. 5(a) displays the photocatalytic removal of TC under visible light. With the photolysis of the TC solution, approximate about 10% of this pollutant degraded within 300 min, indicating its high chemical stability. However, pure GCN degraded about 36% of TC after the same time. After converting GCN to GCN-NSh, the photocatalytic activity improved dramatically. The photocatalytic activity was further improved by coupling Bi_5O_7Br with GCN-NSh, and the GCN-NSh/Bi_5O_7Br (30wt%) nanocomposite presented the highest photocatalytic activity by completely removing this antibiotic after 180 min. Furthermore, Fe-MOF was combined with this photocatalyst to impressively promote the photocatalytic activity of binary GCN-NSh/Bi_5O_7Br (30wt%) nanocomposite, and the photocatalytic performance of the resultant ternary photocatalysts was evaluated as presented in Fig. 5(b). The GCN-NSh/Bi_5O_7Br/Fe-MOF (15wt%) photocatalyst completely degraded TC after 120 min under the same conditions. The impact of the catalyst dosage on the reaction rate was evaluated, and the results are depicted in Fig. 5(c). The TC degradation increased with the dosage of GCN-NSh/Bi_5O_7Br/Fe-MOF (15wt%) from 0.05 to 0.1 g, while high dosages resulted in diminished degradation rate. The decrease in the degradation rate at high doses is relevant to the increase in the turbidity of the suspension, which di-

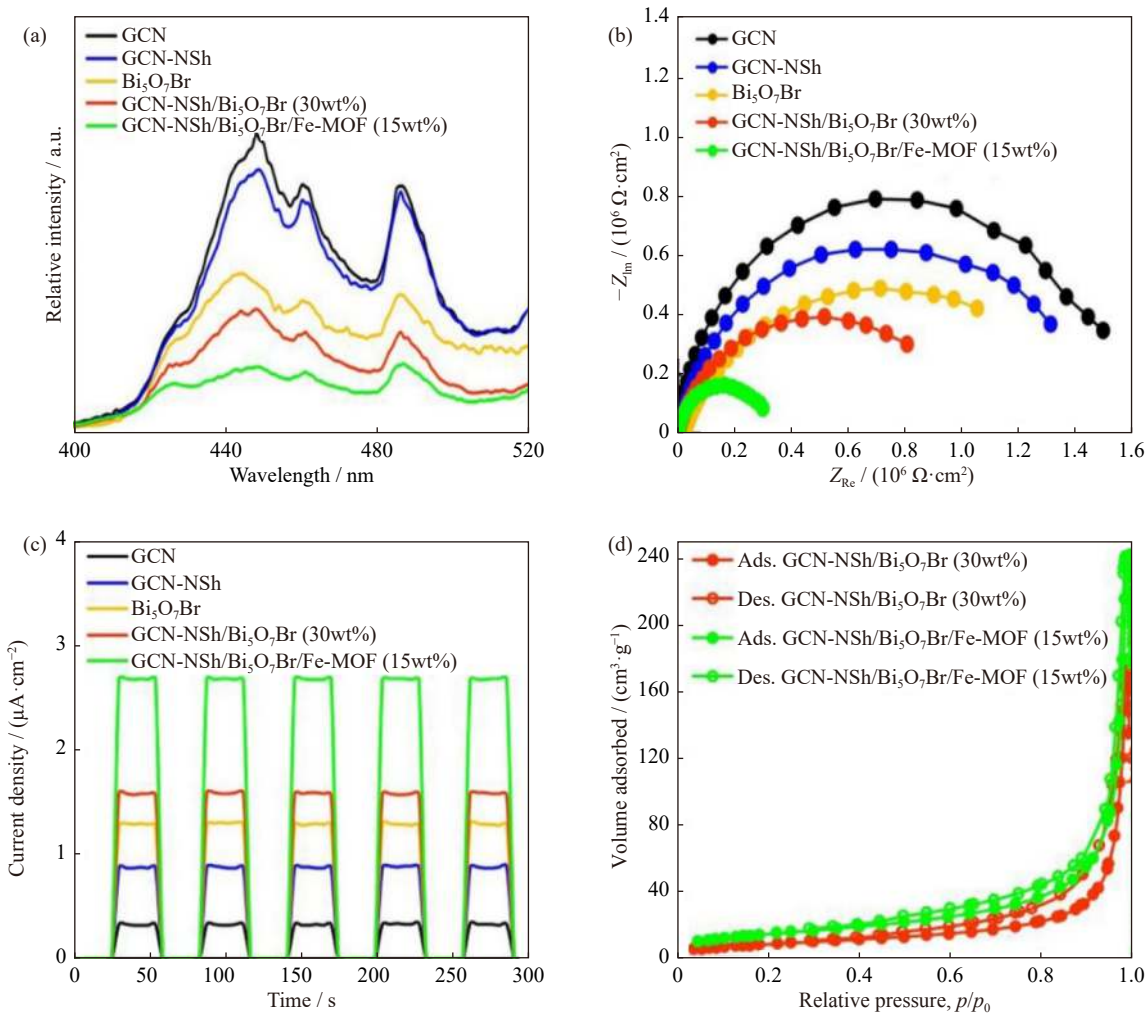

Fig. 4. (a) PL, (b) EIS, (c) photocurrent, and (d) BET data for different photocatalysts.

Table 1. Textural property of the synthesized photocatalysts

Sample	Surface area / ($m^2 \cdot g^{-1}$)	Mean pore diameter / nm	Total pore volume / ($cm^3 \cdot g^{-1}$)
GCN-NSh/Bi_5O_7Br (30wt%)	31.4	34.4	0.2700
GCN-NSh/Bi_5O_7Br/Fe-MOF (15wt%)	54.9	27.2	0.3735

minishes the light entrance of the system. Moreover, the high catalyst dosage leads to photocatalyst accumulation, resulting in the decreased production of active species on the photocatalyst surface. The effect of solution pH on the photocatalytic performance is shown in Fig. 5(d). The photodegradation of TC increased with the decreasing pH up to 3 and then diminished. When the pH decreases, the photoinduced electrons rapidly transfer to the catalyst surface with positive change in acidic solutions, which is beneficial to produce many active $^{\bullet}OH$ and $^{\bullet}O_2^-$ species. However, under acidic conditions, the surface of GCN-NSh/Bi_5O_7Br/Fe-MOF (15wt%) photocatalyst gains positive charges. Owing to the repulsion force between positively charged TC and photocatalyst surface, the contaminant adsorption decreases, leading to diminished activity. The kinetic rate constants for the photocatalytic degradation of TC were calculated according to the pseudo-first-order kinetic equation. Fig. 5(e) presents that among the binary photocatalysts, the GCN-NSh/Bi_5O_7Br (30wt%) sample acquired the highest rate constant of 160×10^{-4} min^{-1}, which is 16.4 and 3.7 folds higher than those of GCN (9.76×10^{-4} min^{-1}) and GCN-NSh (43.25×10^{-4} min^{-1}) photocatalysts, respectively. Among the ternary nanocomposites, the GCN-NSh/Bi_5O_7Br/Fe-MOF (15wt%) nanocomposite shows superior performance. The degradation constant of TC over the optimum ternary photocatalyst is almost 33.06, 7.46, and 2.01 folds higher than those of GCN, GCN-NSh, and GCN-NSh/Bi_5O_7Br (30wt%) photocatalysts, respectively.

Inhibition tests were applied to manifest the role of different active species in TC degradation. Ammonium oxalate (AO), benzoquinone (BQ), and 2-propanol (2-PrOH) radical quenchers were considered as the scavengers of h^+, $^{\bullet}O_2^-$, and $^{\bullet}OH$, respectively [45]. As shown in Fig. 6(a), the rate constant after the addition of AO, BQ, and 2-PrOH diminished to 12.6×10^{-4}, 13.1×10^{-4}, and 149×10^{-4} min^{-1}, respectively. These data show that $^{\bullet}O_2^-$ and h^+ are the dominant species in

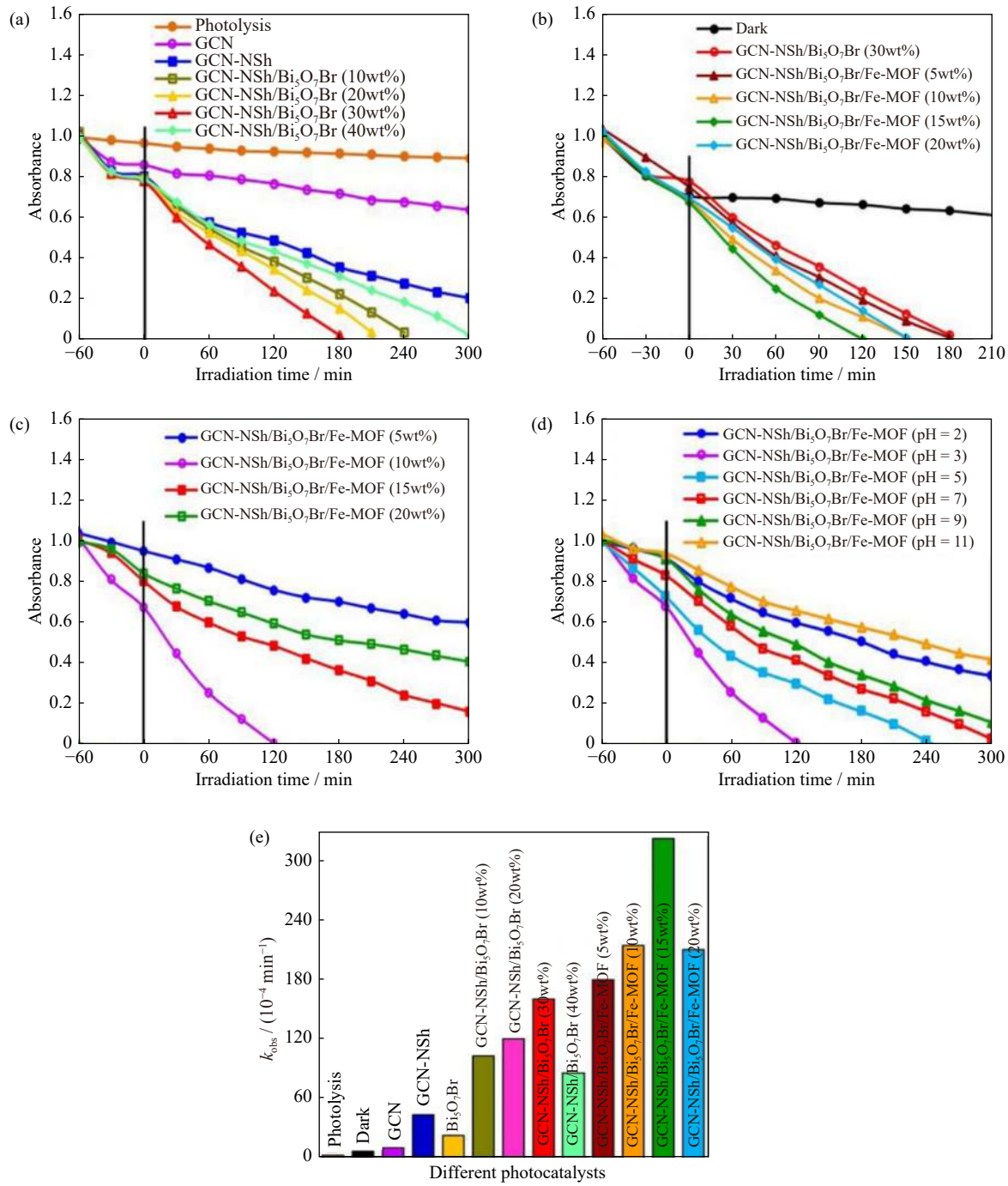

Fig. 5. (a–b) Elimination of TC for different photocatalysts, (c) impact of photocatalyst dosage, (d) effect of pH on the degradation of TC by GCN-NSh/Bi_5O_7Br/Fe-MOF (15wt%) sample, and (e) rate constants observed over the various photocatalysts.

the photocatalytic removal of TC antibiotics. Furthermore, the active species trapping experiments were performed for GCN-NSh, Bi_5O_7Br, and Fe-MOF, and the outcomes are shown in Fig. 6(b), which are in accordance with the results of Fig. 6(a). Mott–Schottky tests were conducted to determine the band energies of GCN-NSh, Bi_5O_7Br, and Fe-MOF samples. As displayed in Fig. 6(c), GCN-NSh, Bi_5O_7Br, and Fe-MOF components present positive slopes, implying that they are n-type materials. Moreover, the flat band potential of GCN-NSh (−1.35 eV vs. Ag/AgCl and −1.15 eV vs. NHE) is more negative than those of Bi_5O_7Br (−0.66 eV vs. Ag/AgCl and −0.46 eV vs. NHE) and Fe-MOF (−0.83 eV vs. Ag/AgCl and −0.63 eV vs. NHE). In the Mott–Schottky curve, the flat band potential is usually considered as the Fermi level of the desired semiconductor, and the conduction band (CB) position is 0.1 eV more negative than the Fermi level. Therefore, the CB positions of GCN-NSh, Bi_5O_7Br, and Fe-MOF samples were −1.25, −0.56, and −0.73 eV, respectively. The valence band (VB) positions were also attained according to $E_{VB} = E_{CB} + E_g$. Hence, the VB positions of GCN-NSh, Bi_5O_7Br, and Fe-MOF were determined to be 1.56, 2.26, and 0.99 eV, respectively.

On the basis of the characterization analyses and the observed impressive photocatalytic performances, a double S-

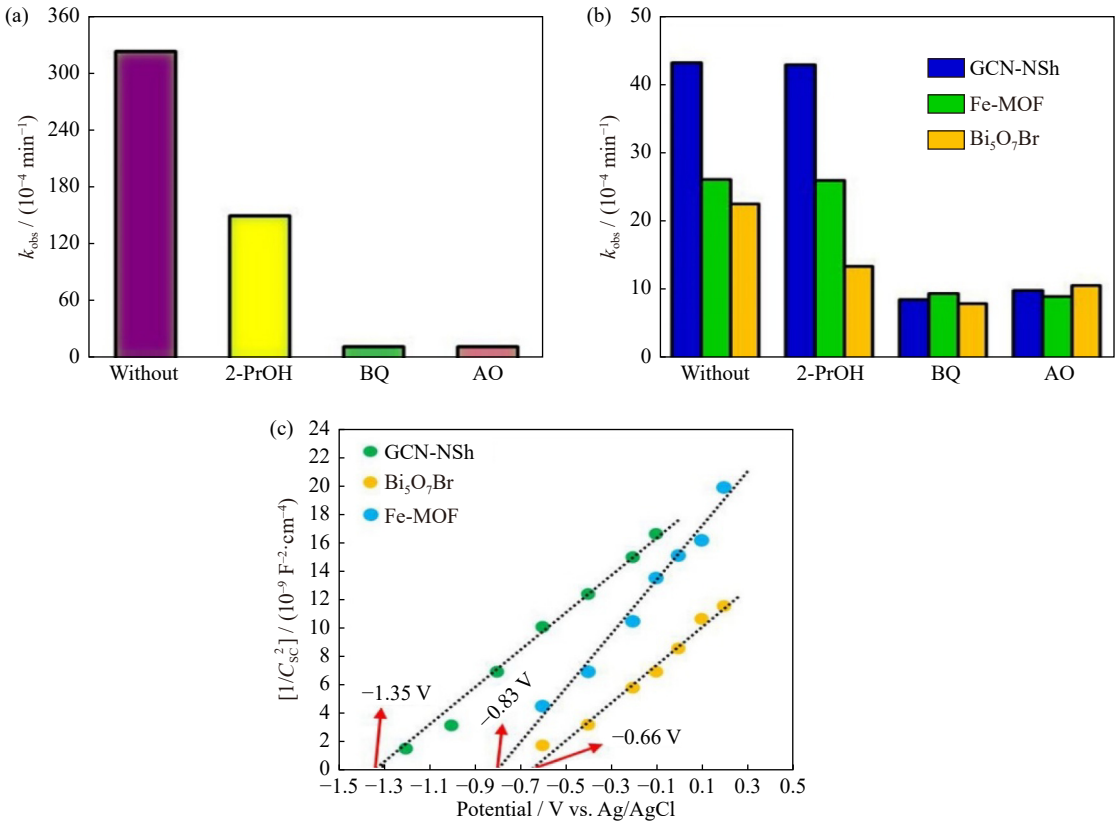

Fig. 6. (a, b) Impact of scavengers on optimal ternary and pure samples, (c) Mott–Schottky data for GCN-NSh, Bi_5O_7Br, and Fe-MOF components.

scheme mechanism for segregation and transfer of charges among the components of the ternary GCN-NSh/Bi_5O_7Br/Fe-MOF nanocomposites was proposed (Fig. 7). The valence band energies (E_{VB}) for GCN-NSh, Bi_5O_7Br, and Fe-MOF were +1.56, +2.26, and +0.99 eV, respectively, and the conduction band energies (E_{CB}) were −1.25, −0.56, and −0.73 eV, respectively [16,29–30]. Furthermore, the energy gaps for GCN-NSh, Bi_5O_7Br, and Fe-MOF were 2.81, 2.82, and 1.72 eV, respectively. As n-type materials, the Fermi energy levels of GCN-NSh, Bi_5O_7Br, and Fe-MOF semiconductors are near their CB levels [29,46–47]. Consequently, the Fermi level of GCN-NSh is more negative than those of Bi_5O_7Br and Fe-MOF components. After heterojunction construction among the components, the electrons tend to migrate from the Fermi level of GCN-NSh to those of Bi_5O_7Br and Fe-MOF components until an equilibrium state was reached.

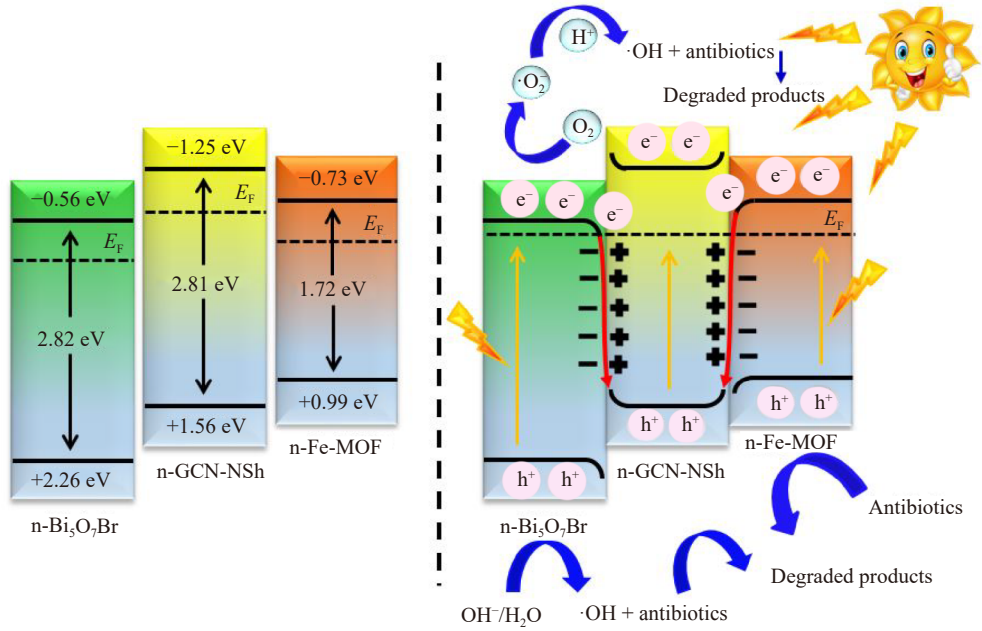

Fig. 7. Mechanism for the degradation of pollutants by ternary GCN-NSh/Bi_5O_7Br/Fe-MOF nanocomposites.

The transfer of electrons among the Fermi levels resulted in the bending of the band edges and the formation of internal electric fields at the interfaces of GCN-NSh/Bi_5O_7Br and GCN-NSh/Fe-MOF [48–49]. Owing to the small band gaps, the electrons on the VB of GCN-NSh, Bi_5O_7Br, and Fe-MOF absorbed visible light to excite their CBs, leaving holes on their VBs. As observed in the scavenging experiments, the generated holes and superoxide anion radicals play a major role in the degradation reaction. The photoinduced electrons in the CB of Bi_5O_7Br and Fe-MOF combined with the holes in the VB of GCN-NSh to reserve the powerful electrons and holes for the production of the mentioned species. Therefore, the accumulated electrons on the CB of GCN-NSh (E_{CB} = −1.25 eV) can produce many $^{\bullet}O_2^-$ species ($E_{O_2/\cdot O_2^-}$ = −0.33 eV), and the holes on the VB of Bi_5O_7Br (E_{VB} = +2.26 eV) can produce many $^{\bullet}OH$ species ($E_{OH^-/\cdot OH}$ = +1.90 eV) and straightly oxidize the pollutants through direct oxidation reactions. Thus, the proposed double S-scheme mechanism not only accelerates the efficient spatial separation of the carriers but also reserves electron/hole pairs with superior redox capabilities, resulting in impressive photocatalytic performance.

The stability and repeated utilization of photocatalysts play a major impact on their widespread utilization. Therefore, the recyclability and stability of GCN-NSh/Bi_5O_7Br/Fe-MOF (15wt%) nanocomposite were measured for 4 successive cycles, and the data are presented in Fig. 8(a). The GCN-NSh/Bi_5O_7Br/Fe-MOF (15wt%) nanocomposite maintained initial ability after four cycles. These outcomes showed that the GCN-NSh/Bi_5O_7Br/Fe-MOF (15wt%) nanocomposite has acceptable reusability under the reaction condition for TC degradation. The XRD and SEM of the GCN-NSh/Bi_5O_7Br/Fe-MOF (15wt%) nanocomposite before photocatalysis and after the 4th run was provided (Fig. 8(b–c)). The phase and structure of the optimum photocatalyst did not change, affirming that the ternary nanocomposite has outstanding durability during degradation. Eventually, three more antibiotics, namely AZY, MET, and CFX, were utilized for the evaluation of the photoactivity of the as-fabricated samples. Fig. 8(d) reveals that compared with pristine GCN, the GCN-NSh/Bi_5O_7Br/Fe-MOF (15wt%) nanocomposite had higher photocatalytic performance in the removal of the selected antibiotics and 36.4, 20.2, and 14.6 times higher activity in the degradation of AZY, MET, and CFX, respectively. Therefore, the GCN-NSh/Bi_5O_7Br/Fe-MOF (15wt%) nanocom-

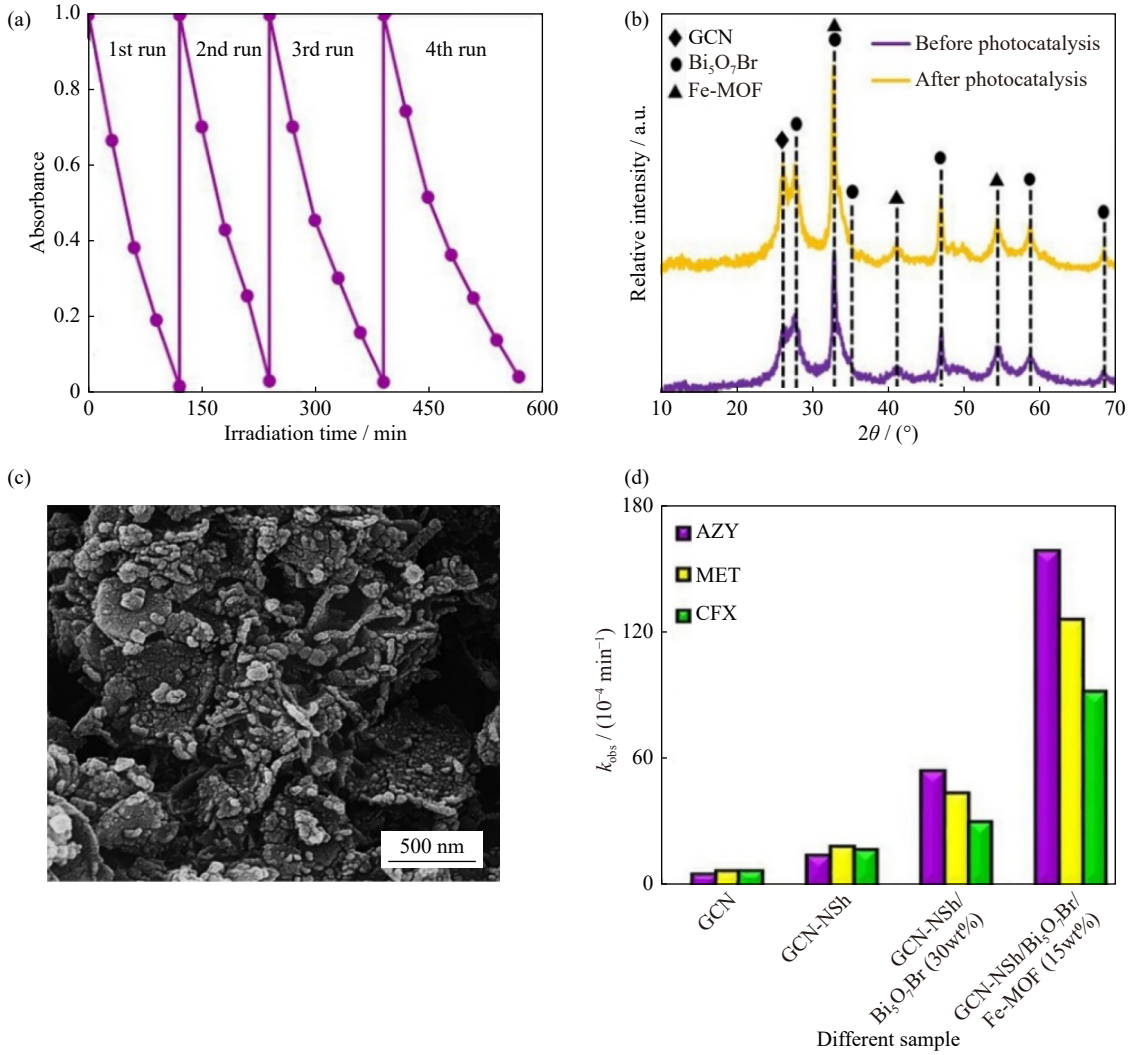

Fig. 8. (a) Recyclability of GCN-NSh/Bi_5O_7Br/Fe-MOF (15wt%) nanocomposite, (b) XRD patterns, and (c) SEM image of the nanocomposite after photocatalysis, and (d) rate constants observed in the degradation of different antibiotics.

posite can be introduced as an encouraging visible-light-induced photocatalyst for the removal of antibiotics in water.

4. Conclusion

This work reported a novel double S-scheme GCN-NSh/Bi_5O_7Br/Fe-MOF photocatalysts using the facile solvothermal procedure. The as-constructed nanocomposites were utilized for the degradation of 4 antibiotics, namely TC, AZY, MET, and CFX, under visible light. The outcomes corroborated that the ability of the GCN-NSh/Bi_5O_7Br/Fe-MOF (15wt%) nanocomposite in the degradation of TC, AZY, MET, and CFX was about 33.06, 36.4, 20.2, and 14.6 folds as high as that of the pristine GCN sample, respectively. The boosted performance of the ternary GCN-NSh/Bi_5O_7Br/Fe-MOF (15wt%) nanocomposite was related to the formation of abundant charge carriers under visible light, effective segregation of charges, less resistance for charge transfer among the components, and extended surface area, leading to improved photocatalytic performance. The impressive photocatalytic performances affirmed that the GCN-NSh/Bi_5O_7 Br/Fe-MOF (15wt%) nanocomposite with developed n–n heterojunctions could be utilized for the degradation of different antibiotics and can produce powerful reactive species through a double S-scheme mechanism for the segregation of charges.

Acknowledgements

Authors are thankful for the supports from the University of Mohaghegh Ardabili and University of Tabriz.

Conflict of Interest

The authors declare no competing financial interests or personal relationships that could affect this paper.

References

[1] L. Xu, H. Zhang, P. Xiong, Q. Zhu, C. Liao, and G. Jiang, Occurrence, fate, and risk assessment of typical tetracycline antibiotics in the aquatic environment: A review, *Sci. Total Environ.*, 753(2021), art. No. 141975.

[2] X.W. Tang, R.D. Tang, S. Xiong, *et al*., Application of natural minerals in photocatalytic degradation of organic pollutants: A review, *Sci. Total Environ.*, 812(2022), art. No. 152434.

[3] C.C. Long, Z.X. Jiang, J.F. Shangguan, T.P. Qing, P. Zhang, and B. Feng, Applications of carbon dots in environmental pollution control: A review, *Chem. Eng. J.*, 406(2021), art. No. 126848.

[4] Y.H. Wen, M.B. Feng, P. Zhang, H.C. Zhou, V.K. Sharma, and X.M. Ma, Metal organic frameworks (MOFs) as photocatalysts for the degradation of agricultural pollutants in water, *ACS EST Eng.*, 1(2021), No. 5, p. 804.

[5] V. Dutta, S. Sharma, P. Raizada, *et al*., An overview on WO_3 based photocatalyst for environmental remediation, *J. Environ. Chem. Eng.*, 9(2021), No. 1, art. No. 105018.

[6] S. Asadzadeh-Khaneghah and A. Habibi-Yangjeh, g-C_3N_4/carbon dot-based nanocomposites serve as efficacious photocatalysts for environmental purification and energy generation: A review, *J. Cleaner Prod.*, 276(2020), art. No. 124319.

[7] M.L. Zhang, Y. Yang, X.Q. An, and L.A. Hou, A critical review of g-C_3N_4-based photocatalytic membrane for water purification, *Chem. Eng. J.*, 412(2021), art. No. 128663.

[8] V. Hasija, V.H. Nguyen, A. Kumar, *et al*., Advanced activation of persulfate by polymeric g-C_3N_4 based photocatalysts for environmental remediation: A review, *J. Hazard. Mater.*, 413(2021), art. No. 125324.

[9] K. Sridharan, S. Shenoy, S.G. Kumar, C. Terashima, A. Fujishima, and S. Pitchaimuthu, Advanced two-dimensional heterojunction photocatalysts of stoichiometric and non-stoichiometric bismuth oxyhalides with graphitic carbon nitride for sustainable energy and environmental applications, *Catalysts*, 11(2021), No. 4, art. No. 426.

[10] P.S. Li, S. Gao, Q.M. Liu, *et al*., Recent progress of the design and engineering of bismuth oxyhalides for photocatalytic nitrogen fixation, *Adv. Energy Sustainability Res.*, 2(2021), No. 5, art. No. 2000097.

[11] D. Mukherjee, B. Van der Bruggen, and B. Mandal, Advancements in visible light responsive MOF composites for photocatalytic decontamination of textile wastewater: A review, *Chemosphere*, 295(2022), art. No. 133835.

[12] Y.H. Wen, P. Zhang, V.K. Sharma, X.M. Ma, and H.C. Zhou, Metal-organic frameworks for environmental applications, *Cell Rep. Phys. Sci.*, 2(2021), No. 2, art. No. 100348.

[13] T.J. Qiu, Z.B. Liang, W.H. Guo, H. Tabassum, S. Gao, and R.Q. Zou, Metal–organic framework-based materials for energy conversion and storage, *ACS Energy Lett.*, 5(2020), No. 2, p. 520.

[14] C. Zhao, X. Pan, Z. Wang, and C.C. Wang, 1 + 1 > 2: A critical review of MOF/bismuth-based semiconductor composites for boosted photocatalysis, *Chem. Eng. J.*, 417(2021), art. No. 128022.

[15] C. Zhang, Y. Li, D. Shuai, Y. Shen, W. Xiong, and L. Wang, Graphitic carbon nitride (g-C_3N_4)-based photocatalysts for water disinfection and microbial control: A review, *Chemosphere*, 214(2019), p. 462.

[16] S. Asadzadeh-Khaneghah, A. Habibi-Yangjeh, D. Seifzadeh, H. Chand, and V. Krishnan, Visible-light-activated g-C_3N_4 nanosheet/carbon dot/FeOCl nanocomposites: Photodegradation of dye pollutants and tetracycline hydrochloride, *Colloids Surf. A*, 617(2021), art. No. 126424.

[17] M. Sabri, A. Habibi-Yangjeh, and A. Khataee, Nanoarchitecturing TiO_2/$NiCr_2O_4$ p–n heterojunction photocatalysts for visible-light-induced activation of persulfate to remove tetracycline hydrochloride, *Chemosphere*, 300(2022), art. No. 134594.

[18] Z. Feng, L. Zeng, Q. Zhang, *et al., In situ* preparation of g-C_3N_4/$Bi_4O_5I_2$ complex and its elevated photoactivity in Methyl Orange degradation under visible light, *J. Environ. Sci.*, 87(2020), p. 149.

[19] M. Wang, P. Guo, Y. Zhang, *et al*., Eu doped g-C_3N_4 nanosheet coated on flower-like $BiVO_4$ powders with enhanced visible light photocatalytic for tetracycline degradation, *Appl. Surf. Sci.*, 453(2018), p. 11.

[20] H.M. Xu, Y.W. Hu, D. Huang, *et al*., Glucose-induced formation of oxygen vacancy and Bi-metal comodified Bi_5O_7Br nanotubes for efficient performance photocatalysis, *ACS Sustainable Chem. Eng.*, 7(2019), No. 6, p. 5784.

[21] F. Chen, H. Wang, H. Hu, *et al*., Construction of NH_2-MIL-101(Fe)/g-C_3N_4 hybrids based on interfacial Lewis acid-base interaction and its enhanced photocatalytic redox capability, *Colloids Surf. A*, 631(2021), art. No. 127710.

[22] D. Gu, S. Zhang, T. Jiang, H. Jiang, X. Wang, and B. Wang, Positive P/g-C_3N_4 thermo-coupled photocatalytic oxidation of refractory organics in wastewater for total utilization of solar Vis-IR region, *Mater. Chem. Phys.*, 253(2020), art. No. 123307.

[23] R. Rajendran, S. Vignesh, A. Sasireka, *et al*., Designing Ag_2O

modified g-C_3N_4/TiO_2 ternary nanocomposites for photocatalytic organic pollutants degradation performance under visible light: Synergistic mechanism insight, *Colloids Surf. A*, 629(2021), art. No. 127472.

[24] N.A. Mohamed, A.F. Ismail, J. Safaei, M.R. Johan, and M.A.M. Teridi, A novel photoanode based on thorium oxide (ThO_2) incorporated with graphitic carbon nitride (g-C_3N_4) for photoelectrochemical water splitting, *Appl. Surf. Sci.*, 569(2021), art. No. 151043.

[25] A. Akulinkin, K. Bolgaru, and A. Reger, Facile synthesis of porous g-C_3N_4/β-SiAlON material with visible light photocatalytic activity, *Mater. Lett.*, 305(2021), art. No. 130788.

[26] Z. Salmanzadeh-Jamadi, A. Habibi-Yangjeh, S.R. Pouran, X.F. Xu, and C.D. Wang, Facile fabrication of TiO_2/Bi_5O_7Br photocatalysts for visible-light-assisted removal of tetracycline and dye wastewaters, *J. Phys. D*, 55(2022), No. 16, art. No. 165105.

[27] B.K. Liu, Y.J. Wu, X.L. Han, J.H. Lv, J.T. Zhang, and H.Z. Shi, Facile synthesis of g-C_3N_4/amine-functionalized MIL-101(Fe) composites with efficient photocatalytic activities under visible light irradiation, *J. Mater. Sci.*, 29(2018), No. 20, p. 17591.

[28] F.P. Zhao, Y.P. Liu, S.B. Hammouda, *et al*., MIL-101(Fe)/g-C_3N_4 for enhanced visible-light-driven photocatalysis toward simultaneous reduction of Cr(VI) and oxidation of bisphenol A in aqueous media, *Appl. Catal. B*, 272(2020), art. No. 119033.

[29] X.Y. Dao, J.H. Guo, Y.P. Wei, F. Guo, Y. Liu, and W.Y. Sun, Solvent-free photoreduction of CO_2 to CO catalyzed by Fe-MOFs with superior selectivity, *Inorg. Chem.*, 58(2019), No. 13, p. 8517.

[30] L. Zhang, X. Yue, J. Liu, *et al*., Facile synthesis of Bi_5O_7Br/BiOBr 2D/3D heterojunction as efficient visible-light-driven photocatalyst for pharmaceutical organic degradation, *Sep. Purif. Technol.*, 231(2020), art. No. 115917.

[31] M. Mousavi and A. Habibi-Yangjeh, Magnetically recoverable highly efficient visible-light-active g-C_3N_4/Fe_3O_4/Ag_2WO_4/AgBr nanocomposites for photocatalytic degradations of environmental pollutants, *Adv. Powder Technol.*, 29(2018), No. 1, p. 94.

[32] J. Zhang, W. Zhang, L. Yue, *et al*., Thiophene insertion and lanthanum molybdate modification of g-C_3N_4 for enhanced visible-light-driven photoactivity in tetracycline degradation, *Appl. Surf. Sci.*, 592(2022), art. No. 153337.

[33] X. Zhou, C. Shao, X. Li, X. Wang, X. Guo, and Y. Liu, Three dimensional hierarchical heterostructures of g-C_3N_4 nanosheets/TiO_2 nanofibers: Controllable growth via gas–solid reaction and enhanced photocatalytic activity under visible light, *J. Hazard. Mater.*, 344(2018), p. 113.

[34] Y.N. Zhu, S.L. Yang, C.Y. Cao, W.G. Song, and L.J. Wan, Controllable synthesis of carbon encapsulated iron phosphide nanoparticles for the chemoselective hydrogenation of aromatic nitroarenes to anilines, *Inorg. Chem. Front.*, 5(2018), No. 5, p. 1094.

[35] P.S. Li, Z.A. Zhou, Q. Wang, *et al*., Visible-light-driven nitrogen fixation catalyzed by Bi_5O_7Br nanostructures: Enhanced performance by oxygen vacancies, *J. Am. Chem. Soc.*, 142(2020), No. 28, p. 12430.

[36] Z. Chen, F. Guo, H. Sun, Y. Shi, and W. Shi, Well-designed three-dimensional hierarchical hollow tubular g-C_3N_4/$ZnIn_2S_4$ nanosheets heterostructure for achieving efficient visible-light photocatalytic hydrogen evolution, *J. Colloid Interface Sci.*, 607(2022), p. 1391.

[37] W. Liu, Y. Li, F. Liu, W. Jiang, D. Zhang, and J. Liang, Visible-light-driven photocatalytic degradation of diclofenac by carbon quantum dots modified porous g-C_3N_4: Mechanisms, degradation pathway and DFT calculation, *Water Res.*, 151(2019), p. 8.

[38] K. Zhao, Z.S. Zhang, Y.L. Feng, S.L. Lin, H. Li, and X. Gao, Surface oxygen vacancy modified Bi_2MoO_6/MIL-88B(Fe) heterostructure with enhanced spatial charge separation at the bulk & interface, *Appl. Catal. B*, 268(2020), art. No. 118740.

[39] Q. Su, J. Li, H. Yuan, *et al*., Visible-light-driven photocatalytic degradation of ofloxacin by g-C_3N_4/NH_2-MIL-88B(Fe) heterostructure: Mechanisms, DFT calculation, degradation pathway and toxicity evolution, *Chem. Eng. J.*, 427(2022), art. No. 131594.

[40] C.P. Bai, J.C. Bi, J.B. Wu, *et al*., Fabrication of noble-metal-free g-C_3N_4-MIL-53(Fe) composite for enhanced photocatalytic H_2-generation performance, *Appl. Organomet. Chem.*, 32(2018), No. 12, art. No. e4597.

[41] L. Wang, W. Zhang, Y. Su, Z. Liu, and C. Du, Halloysite derived 1D mesoporous tubular g-C_3N_4: Synergy of template effect and associated carbon for boosting photocatalytic performance toward tetracycline removal, *Appl. Clay Sci.*, 213(2021), art. No. 106238.

[42] Y.J. Wang, Q.Y. Wang, H. Zhang, *et al*., CTAB-assisted solvothermal construction of hierarchical Bi_2MoO_6/Bi_5O_7Br with improved photocatalytic performances, *Sep. Purif. Technol.*, 242(2020), art. No. 116775.

[43] R. Tang, S.J. Zhou, H. Li, R. Chen, L.Y. Zhang, and L.W. Yin, Halogen bonding induced aqueously stable CsPbBr3@MOFs-derived Co_3O_4/N-doped-C heterostructure for high-performance photoelectrochemical water oxidation, *Appl. Catal. B*, 265(2020), art. No. 118583.

[44] A.G. Ramu, S. Salla, S. Chandrasekaran, *et al*., A facile synthesis of metal ferrites and their catalytic removal of toxic nitro-organic pollutants, *Environ. Pollut.*, 270(2021), art. No. 116063.

[45] Y. Liu, H.G. Guo, Y.L. Zhang, *et al*., Heterogeneous activation of persulfate for Rhodamine B degradation with 3D flower sphere-like BiOI/Fe_3O_4 microspheres under visible light irradiation, *Sep. Purif. Technol.*, 192(2018), p. 88.

[46] X.C. Yu, Z.Y. Song, X.Q. Dong, *et al*., Enhanced photocatalytic activity of rare earth (Yb, Nd and Ce)-doped g-C_3N_4 nanosheets for the degradation of organic dyes under visible light, *J. Mater. Sci.*, 33(2022), No. 16, p. 13271.

[47] F. Xie, Q. Xi, H. Li, *et al*., Two-dimensional/two-dimensional heterojunction-induced accelerated charge transfer for photocatalytic hydrogen evolution over Bi_5O_7Br/Ti_3C_2: Electronic directional transport, *J. Colloid Interface Sci.*, 617(2022), p. 53.

[48] P.F. Xia, S.W. Cao, B.C. Zhu, *et al*., Designing a 0D/2D S-scheme heterojunction over polymeric carbon nitride for visible-light photocatalytic inactivation of bacteria, *Angew. Chem. Int. Ed.*, 59(2020), No. 13, p. 5218.

[49] F. He, B.C. Zhu, B. Cheng, J.G. Yu, W. Ho, and W. Macyk, 2D/2D/0D TiO_2/C_3N_4/Ti_3C_2 MXene composite S-scheme photocatalyst with enhanced CO_2 reduction activity, *Appl. Catal. B*, 272(2020), art. No. 119006.